Article

Enhancement of Wear Resistance on H13 Tool and Die Steels by Trace Nanoparticles

Shu-Qing Kou, Jun-Nan Dai, Wen-Xin Wang *, Chun-Kai Zhang, Si-Yu Wang, Tai-Yu Li and Fang Chang *

Key Laboratory of Automobile Materials, Ministry of Education and Department of Materials Science and Engineering, Jilin University, Changchun 130025, China; kousq@jlu.edu.cn (S.-Q.K.); daijn19@mails.jlu.edu.cn (J.-N.D.); zhangck1620@mails.jlu.edu.cn (C.-K.Z.); wangsy1620@mails.jlu.edu.cn (S.-Y.W.); licd21@mails.jlu.edu.cn (T.-Y.L.)
* Correspondence: wangwx1620@mails.jlu.edu.cn (W.-X.W.); changfang@jlu.edu.cn (F.C.)

Abstract: In order to improve the impact toughness and wear resistance of the tool and die steels, this study innovatively prepared strengthened H13 steels with different contents of single-phase TiC and dual-phase $TiC + TiB_2$ through in situ nanoparticle/Al master alloys at room temperature. The microstructure evolution and mechanical properties as well as wear resistance were investigated. Results indicate that the H13 steel with 0.02 wt.% dual-phase $TiC + TiB_2$ nanoparticles has a more uniform and finer microstructure, and the mechanical properties and wear resistance are significantly improved. The yield strength, maximum tensile strength, breaking strain, uniform elongation, product of strength plasticity, and unnotched and U-notched impact toughness of H13 steel with 0.02 wt.% dual-phase $TiC + TiB_2$ are higher than that of H13 steel. In addition, the volume wear rate, maximum scratch depth and width reach 7.1×10^{-11} m^3/m, 6050 nm and 90 μm, respectively, which are reduced by 44.5%, 30.1% and 45.5% compared with that of H13 steel. Refining the microstructure and improving impact toughness and wear resistance of H13 tool steel through trace nanoparticles can provide important inspiration for industrial applications.

Keywords: H13; nanoparticles; manipulate; microstructure; abrasive wear; mechanism

1. Introduction

Tool and die steels should not only ensure wear resistance, but also need good impact toughness, which can guarantee that they have a long service life under wear conditions [1–5]. For example, the shield machine rolling tools generally made of tool and die steels with high Cr content [6–11] have good mechanical properties represented by impact toughness, as well as high wear resistance [12–14]. The main reason is that when the rolling tool is used for rock rolling, it bears the abrasive wear condition under high stress, and a large amount of heat is generated by instantaneous friction, which makes the tool surface temperature rise rapidly [15–17]. After rotating, the tool surface immediately is cooled down by water spray. Therefore, the tool not only withstands the wear condition [18–20], but also bears the cold and hot fatigue. However, for some tool and die steels with specific compositions, wear resistance and impact toughness are contradictory. Under the condition of high wear resistance, the impact toughness of steels is generally poor [21–24]. Therefore, it is necessary to balance the impact toughness and wear resistance in order to improve the service life of the tools [25–27]. Generally speaking, there are many methods to improve the contradictory mechanical properties of steel, such as ultra-pure purification, heat treatment, large forging ratio and so on [21,28–31]. However, on a technical level, the tool and die steel for cutting tools has reached a certain limit. Therefore, developing a new and efficient method that can improve the impact toughness and wear resistance of steels has a high practical significance and industrial application value [32–34].

Recent studies have found that nanoparticles can not only nucleate and refine the solidification microstructures of an alloy [35–38], but also increase the strength and toughness

of alloys [39–43]. Nanoparticles have a strong effect of microstructure refinement [44–46]. Nanoparticles not only can refine the microstructure and control the growth size and morphology of grains [47–51], but also greatly improve the comprehensive mechanical properties of the alloys, especially, high-temperature strength, high-temperature creep, high-temperature wear resistance, impact toughness and fatigue [52–57]. Compared with traditional strengthening and toughening technology, the effective control technology by nanoparticles has significant advantages such as not changing the existing casting process and equipment, green and environmental protection [58–60]. At present, there are few studies on the microstructure evolution and anti-wear behaviors of tool steels manipulated by trace nanoparticles. It is necessary to study the anti-wear behavior and its mechanism of steels manipulated by trace nanoparticles.

However, it is difficult to add nanoparticles to liquid steel [35,47,61,62] due to the large specific gravity difference between liquid steel and nanoparticles [63–67]. Nanoparticles easily adsorb contamination and thus affect the strengthening effect [68,69]. In addition, the surface energy of nanoparticles is relatively high, so they are easy to agglomerate and difficult to disperse [70–72]. Non-dispersed and surface-polluted nanoparticles not only fail to strengthen, but also deteriorate the properties of the steel. In order to successfully prepare the nanoparticle reinforced steels, this work focuses on adding nanoparticles to the liquid steel through the in situ nanoparticle/Al master alloys. The effects of different types and contents of nanoparticles on the microstructures and their corresponding wear resistance were studied. Enhancement and mechanism of wear resistance of H13 tool and die steels manipulated by trace nanoparticles were analyzed. This method can significantly refine the microstructures and improve the wear resistance of H13 tooling steels through trace nanoparticles, which provides a new method for improving the wear resistance of high-performance alloys and has important influence for industrial applications.

2. Materials and Methods

2.1. Preparation of H13 Tool and Die Steels Manipulated by Trace Nanoparticles

The in situ nanoparticle/Al master alloys are prepared by self-propagating combustion in Al-Ti-C/B_4C systems. The specific preparation process is reported in previous research [73–75]. The three powders of Al, Ti, and B were mechanically ground in a ball mill, and then cold-pressed into a cylindrical shape. Then, the specimens were hot-pressed and vacuum-sintered to initiate a combustion synthesis reaction, and cooled to room temperature to obtain a master alloy. The chemical composition of H13 tool and die steels manipulated by trace nanoparticles is shown in Table 1. The preparation process of H13 tool and die steels manipulated by trace nanoparticles is shown in Figure 1. The steel is melted in an intermediate frequency induction furnace and the molten steel is discharged at 1873 K. At the same time, the in situ nanoparticle/Al master alloys enter the ladle with the liquid steel, and then aluminum matrix melts in liquid steel and nanoparticles are gradually released. The mass of molten steel is 1000 kg and the master alloy is 333 g or 666 g, and the corresponding content of the nanoparticles is 0.01 wt.% or 0.02 wt.%, that is, 100 g or 200 g. The mass of Al is 233 g or 466 g, and the mass ratio of nanoparticles to Al is 3:7. The pre dispersed in situ nanoparticles in the aluminum are wrapped by the melt and master alloy, so they cannot contact the air and their surfaces are also not contaminated. When the master alloys enter the ladle with the liquid steel, it is added to the liquid steel with the liquid flow. At the same time, the aluminum matrix melts in liquid steel and gradually releases nanoparticles, thus making nanoparticles evenly distributed in liquid steel.

Table 1. The chemical composition of H13 tool and die steels.

Sample	C	Cr	Mo	V	Si	Mn	P	S	Fe
H13	0.41	5.5	1.75	1.20	1.20	0.50	<0.03	<0.03	Bal.
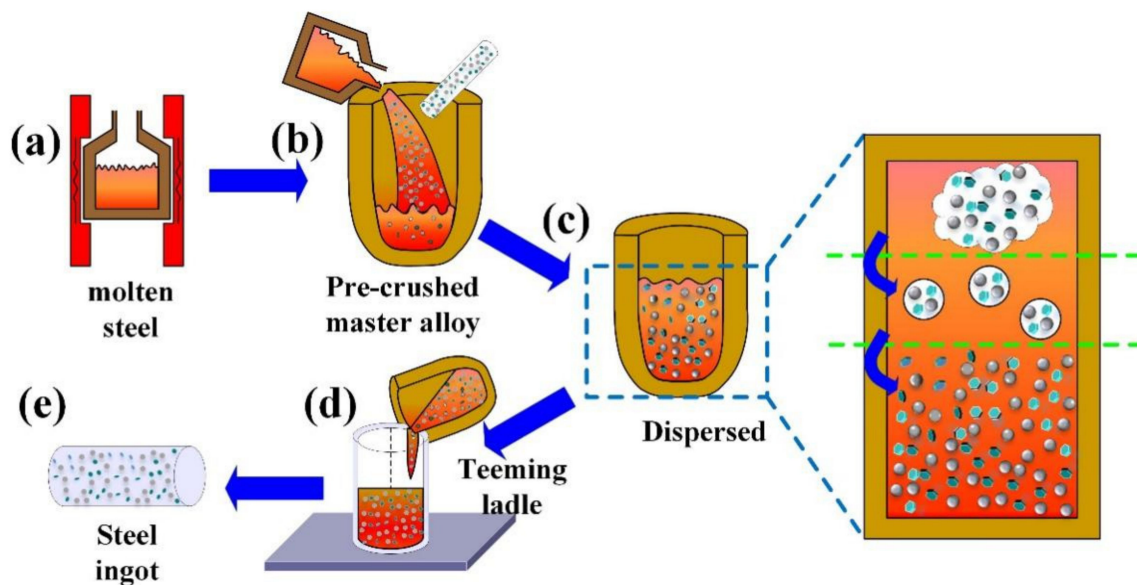
Figure 1. The preparation process of H13 tool and die steels manipulated by trace nanoparticles: (**a**) melt, (**b**) addition and release of nanoparticles, (**c**) uniform distribution of nanoparticles, (**d**) casting, (**e**) steel ingot.

This process solves the problem of agglomeration of nanoparticles, thus making nanoparticles evenly distributed in liquid steel. The molten steel in the ladle is purified by argon blowing for 5 min. Then, the liquid steel is cast into a billet through a mold. After that, the billet is subjected to electroslag remelting, homogenization, forging, grain refinement and tempering. Finally, H13 tool and die steels manipulated by trace nanoparticles are quenched at 1313 K and tempered three times in the furnace at 803 K, 813 K, and 823 K, respectively. The microstructures of tempered martensite are obtained.

## 2.2. Characterization and Performance Testing

The microstructure was observed by optical microscope (OM, AXIO-Imager A2 Microscope, Oberkochen, Germany), scanning electron microscope (SEM, Tescan vega3 XM, Brno, Czech Republic) with electron backscatter diffraction (EBSD, Oxford NordlysMax EBSD, Oxford, UK) and transmission electron microscope (TEM, JEM-2100F, Tokyo, Japan); corrosion treatment was carried out with 10% nitric acid alcohol solution before observation. Impact tests were conducted using an ITM impact testing machine (JBDW-500CY, Jinan, China) to test the impact toughness of the H13 tool and die steels. Unnotched impact specimens with dimensions of $10 \times 7 \times 55$ mm^3 and U-notch impact specimens with dimensions of $10 \times 10 \times 55$ mm^3 were prepared for the impact test. Tensile tests were performed at a strain rate of 10^{-4} s^{-1} on a servo-hydraulic materials testing system (MTS, MTS 810, Eden Prairie, MN, USA).

As shown in Figure 2, the abrasive wear experiment was conducted on the wheel wear tester (MLH-30, Zhangjiakou, China). The samples with the dimension of 35 mm $\times$ 5 mm $\times$ 5 mm cuboid are used. The size of wear surface is 35 mm $\times$ 5 mm. The abrasive particle sizes of sandpaper are 28 μm and 14 μm, and the loads are 15 N and 25 N. After one pass of each portion of the sample on the sandpaper, it will be replaced with a new sandpaper. The wear distance of every specimen is 150 m. The samples before and after wear test were weighed using a balance with an accuracy of 0.0001 g and the volume wear rate is calculated as:

$$W = \frac{\Delta m}{\rho L} \tag{1}$$

where W is the volume wear rate (m^3/m), Δm is the difference between the mass of the sample before and after wear (g), ρ is the density of the sample (kg/m^3), which was

measured by the electronic densitometer (WLD-3005, Shenzhen, China), *L* is the total stroke of wear (m).
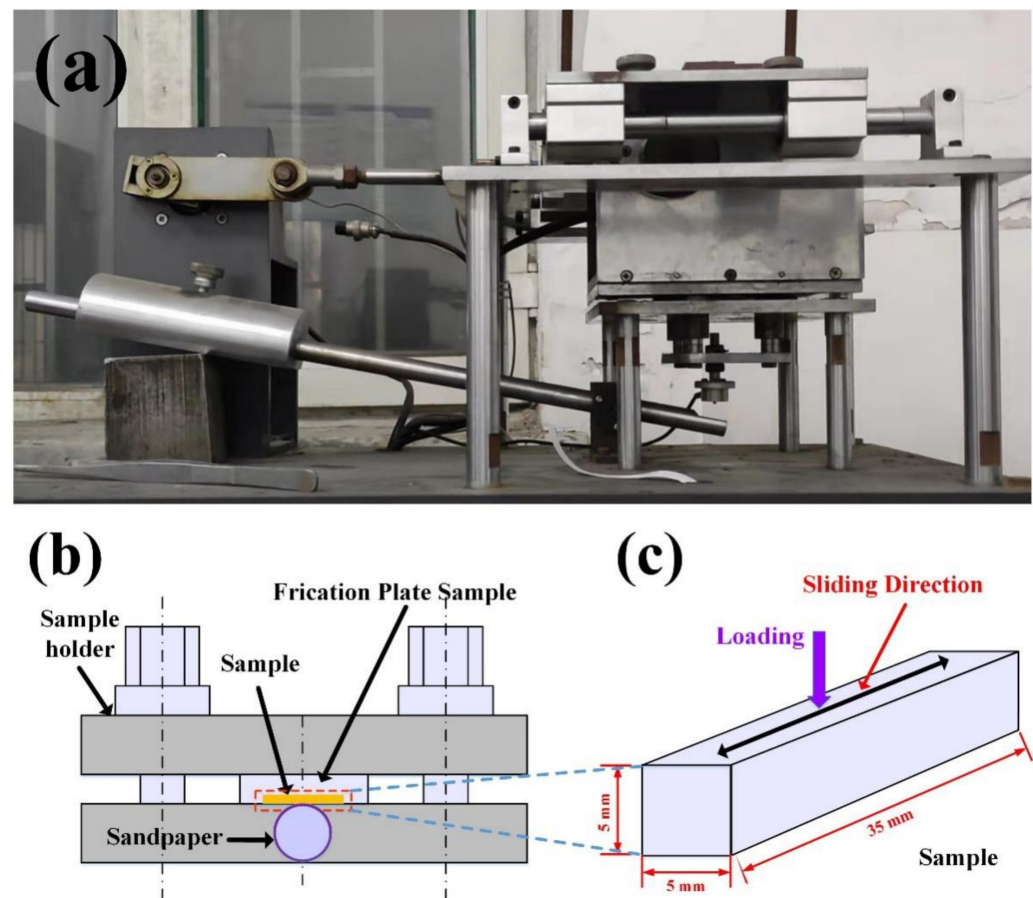
Figure 2. Schematic diagram of abrasive wear process: (**a**) machine, (**b**) sample stage, (**c**) wear direction and sample size.

The optical profiler (NT9100, VEECO, Sacramento, CA, USA) was used to characterize the structural features of the specimen after wear under different conditions. Each experiment was performed at least three times, and the surface roughness value is the average value of the three tests.

3. Results and Discussion

3.1. Microstructure of H13 Steels Manipulated by Trace Nanoparticles

Figure 3 shows the microstructure of H13 steels without and with different types and contents of nanoparticles under optical microscope. As shown in Figure 3a, tempered lath martensite, carbide and a small amount of residual austenite are observed after quenching and tempering heat treatment. Figure 3b shows the metallographic microstructure of H13 with 0.02 wt.% TiC nanoparticles. It can be seen that the distribution of martensite becomes more uniform and smaller because of the addition of TiC nanoparticles. The distribution of black lath area is more uniform, indicating that lath martensite is refined. At the same time, the size of regular white granular retained austenite decreases, and no carbide segregation at grain boundary is found. As shown in Figure 3c,d, the addition of dual phase nanoparticles has the same effect for the metallographic microstructures of H13 as single-phase nanoparticles. The martensite becomes finer and smaller, residual austenite becomes smaller, and also no carbide segregation at the crystal boundary is found. This trend of carbide segregation becomes more obvious with the further increase of the content of dual phase nanoparticles.
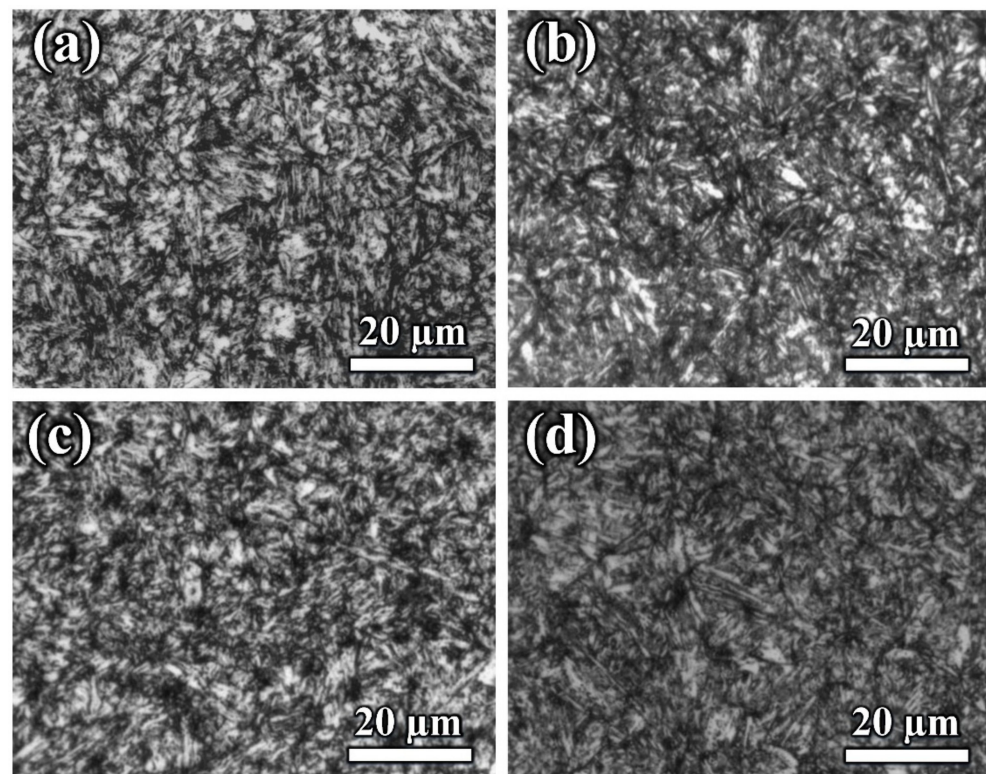
Figure 3. Heat-treated microstructure of H13 steels without and with different types and contents of nanoparticles under optical microscope: (**a**) H13; (**b**) 0.02 wt.% TiC; (**c**) 0.01 wt.% TiC+ TiB_2; (**d**) 0.02 wt.% TiC + TiB_2.
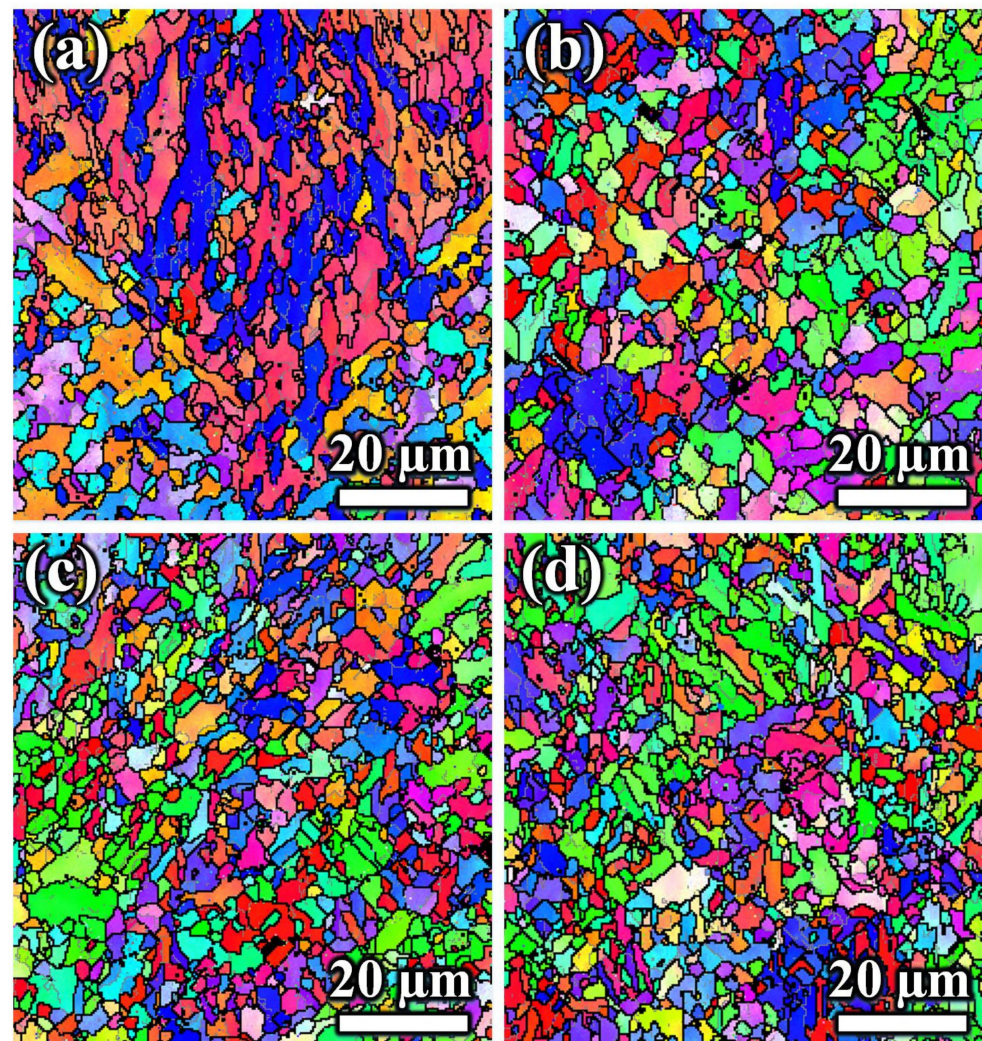
Figure 4 shows EBSD images of H13 steels without and with different nanoparticles. It can be seen from Figure 4a that there are a large number of coarse and straight grains in the H13 steel without nanoparticles; the grain size is mainly between 10 μm and 20 μm with certain directionality and uneven distribution. The grains of H13 steel with 0.02 wt.% single-phase TiC nanoparticles (Figure 4b) are obviously refined and most of the grains do not exceed 10 μm in size. In addition, the shape is relatively full and the directionality basically disappears. The grains of H13 steel with 0.01 wt.% (Figure 4c) and 0.02 wt.% (Figure 4d) dual-phase TiC + TiB_2 nanoparticles are more refined, most of the grains do not exceed 5 μm in size, and the distribution is relatively uniform. These results indicate that trace nanoparticles have a refinement on the microstructures of H13 steels, but the refinement effect of the dual-phase nanoparticles is more obvious. Figure 5 shows TEM images of H13 steel and H13 steel manipulated by 0.02 wt.% TiC + TiB_2. It can be seen that the addition of nanoparticles refines the martensitic lath in H13 steel and the carbides in martensite become smaller in size and greater in quantity. Moreover, the nanoparticles effectively hindered the growth of lath martensite and made the precipitation of carbides more uniform. The dense microstructures with fine and uniform particles can provide the necessary conditions for H13 steels to have better mechanical properties.

### 3.2. Mechanical Properties of H13 Steels Manipulated by Trace Nanoparticles

Table 2 gives the tensile and impact toughness values of different types and contents of nanoparticle-reinforced H13 steel at room temperature. The hardness, yield strength, maximum tensile strength, fracture strain, uniform elongation and product of strength plasticity of H13 steel are 46.9 HRC, 1023 MPa, 1325 MPa, 14.8%, 5.3% and 16,348 MPa %, respectively. For the H13 steel with 0.02 wt.% single-phase TiC nanoparticles and the H13 steel with 0.01 wt.% dual-phase TiC + TiB_2 nanoparticles, these properties were slightly improved. However, the hardness, yield strength, maximum tensile strength, fracture strain, uniform elongation and product of strength plasticity of H13 steel with 0.02 wt.%

dual-phase TiC + TiB$_2$ nanoparticles increased by 3.8%,11.6%, 7.6%, 14.2%, 64.2% and 26.4%, respectively, compared to H13. Therefore, the hardness, yield strength, maximum tensile strength and product of strength plasticity of dual-phase TiC + TiB$_2$ nanoparticle-reinforced H13 steel can be strengthened with the increase of the content of nanoparticles and the fracture strain as well as uniform elongation, which are also significantly improved compared to unreinforced H13 steel. Furthermore, the H13 steel manipulated by dual-phase nanoparticles enhances the uniform elongation of H13 steel, which promotes H13 steel to have more uniform and stable plastic deformation.

Figure 4. EBSD images of H13 steels without and with different types and contents of nanoparticles: (**a**) H13, (**b**) 0.02 wt.% TiC, (**c**) 0.01 wt.% TiC + TiB$_2$ and (**d**) 0.02 wt.% TiC + TiB$_2$.
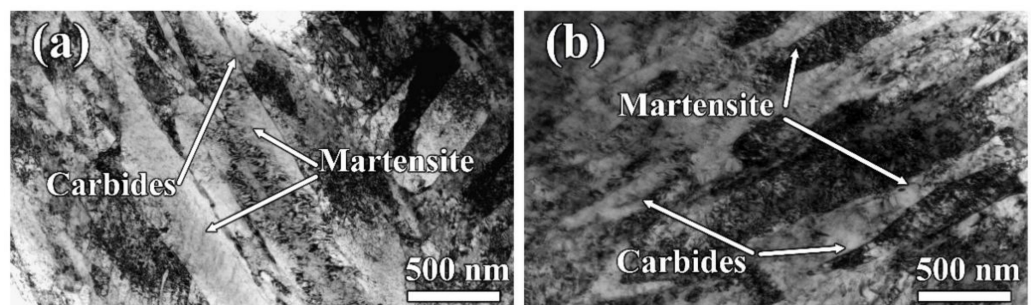
Figure 5. TEM morphologies of (**a**) H13 steel and (**b**) H13 steel manipulated by 0.02 wt.% TiC + TiB$_2$.

Table 2. Tensile properties and impact toughness of H13 steels without and with different contents of nanoparticles at room temperature.

| Sample	Hardness (HRC)	σ0.2 (MPa)	σUTS (MPa)	εf (%)	UE (%)	Product of Strength Plasticity (MPa·%)	Non-NotchedImpact Toughness (J/cm²)	U-Notched Impact Toughness (J/cm²)
H13	46.9 ± 0.1	1023 ± 6	1325 ± 7	14.8 ± 0.2	5.3 ± 0.2	16,348 ± 340	332.9 ± 2.4	30.94 ± 0.6
H13 + 0.02 wt.% TiC	47.5 ± 0.2	1131 ± 8	1415 ± 5	16.8 ± 0.4	5.6 ± 0.3	19,835 ± 325	406.8 ± 3.1	33.93 ± 1.3
H13 + 0.01 wt.% TiC + TiB₂	48.2 ± 0.1	1035 ± 6	1343 ± 6	17.2 ± 0.2	8.9 ± 0.3	19,989 ± 296	419.6 ± 3.3	38.46 ± 0.8
H13 + 0.02 wt.% TiC + TiB₂	48.7 ± 0.1	1142 ± 12	1426 ± 15	16.9 ± 1.2	8.7 ± 0.5	20,662 ± 492	449.3 ± 2.9	41.39 ± 1.0

In addition, the non-notched and U-notched impact toughness of H13 steel without nanoparticles reached 332.9 J/cm² and 30.94 J/cm², respectively. After adding 0.02 wt.% single-phase TiC, 0.01 wt.% dual-phase TiC + TiB₂ and 0.02 wt.% dual-phase TiC + TiB₂ nanoparticles to H13 steel, the non-notched and U-notched impact toughness were 406.8 J/cm² and 33.93 J/cm², 419.6 J/cm² and 38.46 J/cm², 449.3 J/cm² and 41.39 J/cm², respectively, which increased by 22.2% and 9.6%, 26.0% and 24.3%, 35.0% and 33.8%, respectively, compared with H13 steel without nanoparticles. The H13 steel with 0.02 wt.% dual-phase nanoparticles has larger impact toughness and a more uniform and finer microstructure, thus it has a better performance during plastic deformation. Furthermore, the cracks caused by the reduction in grain size consume more energy during propagation.

Adding single-phase TiC and dual-phase TiC + TiB₂ nanoparticles can improve the performance of H13 steel to a certain extent. Especially, the addition of 0.02 wt.% dual-phase TiC + TiB₂ nanoparticles enhances the yield strength and tensile strength of H13 steel the most, simultaneously with the highest impact toughness and the best wear resistance. Adding nanoparticles to H13 steel makes the grain size of the refined and the distribution of grains more uniform and dense. While the H13 steel is subjected to external force, the better coordination between finer grains can disperse the stress and effectively prevent stress concentration, thereby improving the performance of the steel. By comparison, the dual-phase TiC + TiB₂ nanoparticles have a more obvious strengthening effect on steel. H13 steel manipulated by dual-phase TiC + TiB₂ nanoparticles has finer lath martensite and denser microstructure than that of single-phase TiC nanoparticles, so that it has good mechanical properties and impact toughness. The added nanoparticles can be used as nucleation sites to promote nucleation and inhibit the growth of martensite, which makes the microstructure of H13 steel finer and the grain boundaries increase, thus playing a role in strengthening. Similar studies have been reported in the literature [5,25,42,64,65]. The existence of uniformly dispersed carbides can effectively hinder the movement of dislocations and the grain boundaries of the refined H13 steel increase, which is not conducive to the expansion of cracks. These synergistic effects improve the mechanical properties of the H13 steel with different types and contents of nanoparticles. Overall, the main strengthening mechanisms can be attributed to grain refinement strengthening and second-phase strengthening.

3.3. Abrasive Wear Behavior of H13 Steel Manipulated by Trace Nanoparticles

Figure 6 and Table 3 show the volumetric wear rate of H13 steels without and with different types and contents of nanoparticles under sandpaper with abrasive particle size of 28 μm and the loads of 15 N and 25 N at room temperature. It can be seen that the volumetric wear rate of the different materials increases with the increase in load. When the load is 15 N, the volumetric wear rate of H13 steel with 0.02 wt.% TiC, 0.01 wt.% TiC + TiB₂ and 0.02 wt.% TiC + TiB₂ is reduced by 48.3%, 35.6% and 52.9%, respectively, compared with H13 steel without nanoparticles. Further, when the load is 25 N, the volumetric wear rate of H13 steel with 0.02 wt.% TiC, 0.01 wt.% TiC + TiB₂ and 0.02 wt.% TiC + TiB₂ are respectively reduced by 38.3%, 28.9% and 44.5% compared to H13 steel without nanoparticles. Compared to single-phase nanoparticles, dual-phase nanoparticles have a better effect on improving wear resistance.
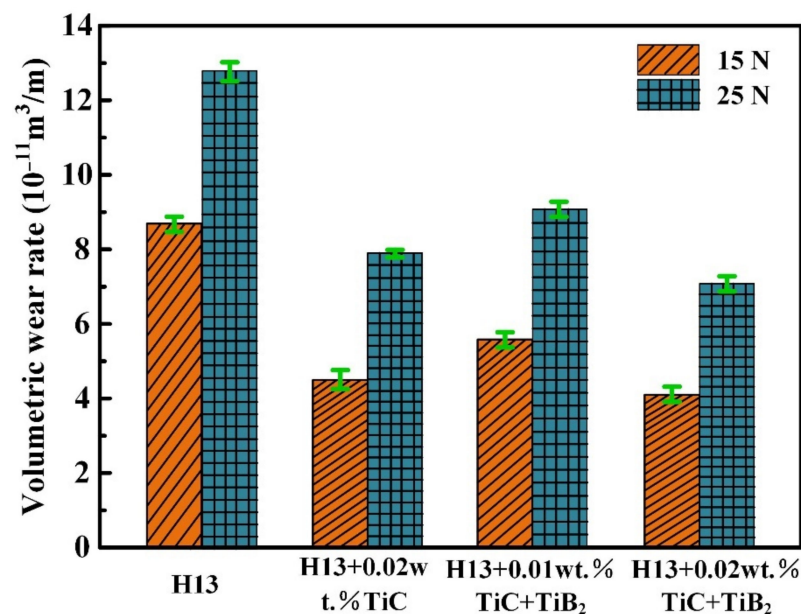
Figure 6. Volumetric wear rate of H13 steel without and with different types and contents of nanoparticles under sandpaper with abrasive particle size of 28 μm and different loads.
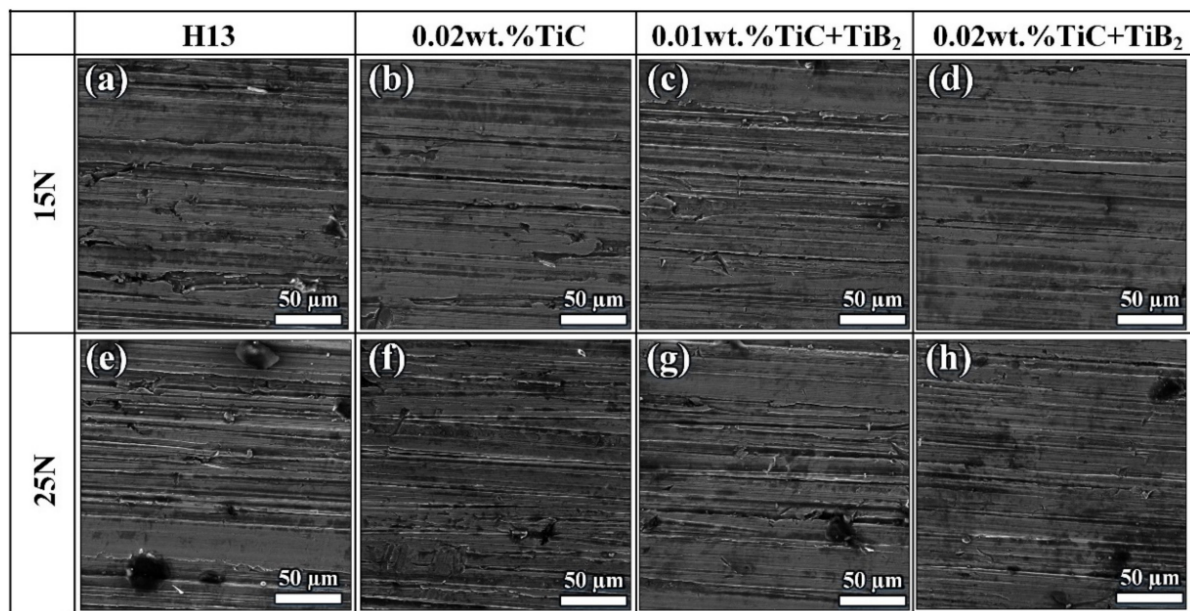
Table 3. Volumetric wear rate of H13 steel without and with different types and contents of nanoparticles under sandpaper with abrasive particle size of 28 μm and different loads.

Sample	Weight Loss (g)		Volumetric Wear Rate (10^{-11} m^3/m)	
	15N	25N	15N	25N
H13	0.1024 ± 0.0023	0.1507 ± 0.0037	8.7 ± 0.2	12.8 ± 0.3
H13 + 0.02 wt.% TiC	0.0530 ± 0.0035	0.0930 ± 0.0011	4.5 ± 0.3	7.9 ± 0.1
H13 + 0.01 wt.% TiC + TiB$_2$	0.0659 ± 0.0019	0.1072 ± 0.0021	5.6 ± 0.2	9.1 ± 0.2
H13 + 0.02 wt.% TiC + TiB$_2$	0.0483 ± 0.0016	0.0836 ± 0.0018	4.1 ± 0.2	7.1 ± 0.2

Figure 7 shows the SEM micrographs of the abrasive worn surface of H13 steel without and with different types and contents of nanoparticles under the loads of 15 N and 25 N. It can be seen from Figure 7a that many deeper and wider furrows on the surface wear of H13 steel without nanoparticles are observed. However, the width of the furrow on the surface wear of H13 steel with 0.02 wt.% single-phase TiC nanoparticles is significantly reduced (Figure 7b). Compared with H13 steel with 0.02 wt.% single-phase TiC nanoparticles, the surfaces of H13 steel with 0.01 wt.% dual-phase TiC + TiB$_2$ nanoparticles have more furrows and a greater degree of surface wear but this is much less severe than that of the H13 steel matrix (Figure 7c). Surprisingly, the H13 steel with 0.02 wt.% dual-phase TiC + TiB$_2$ nanoparticles has the mildest surface wear and the smallest depth and width of furrow (Figure 7d). While under a load of 25 N, as shown in Figure 7e–h, the wear characteristic of different types and contents of the steel is similar to that under the load of 15 N. However, it is obvious that the degree of wear of different materials under this load are more severe than that under the load of 15 N. The increase in load increases the interaction strength between the steel and the sandpaper, which leads to an increase in the degree of wear. In general, trace nanoparticle-reinforced H13 steel can effectively reduce the depth and width of the furrows on the surface of the steel and enhance the wear resistance of the steel. The enhancement effect of 0.02 wt.% single-phase TiC nanoparticles on the wear resistance of H13 steel is greater than that of 0.01 wt.% dual-phase TiC + TiB$_2$ nanoparticles. Furthermore, the H13 steel with 0.02 wt.% dual-phase TiC + TiB$_2$ nanoparticles has the best wear resistance, indicating that the enhancement effect of dual-phase nanoparticles on the wear resistance of steel is much greater than that of single-phase nanoparticles at the same content. The reason is that the hardness, strength and toughness of bidirectional

nanoparticle-strengthened steel are much higher than that of H13 steel, which guarantee its higher wear resistance.

Figure 7. SEM of worn surface of H13 steels without and with nanoparticles under sandpaper with abrasive particle size of 28 μm and different loads: (**a–d**) 15N and (**e–h**) 25 N.

Figure 8 and Table 4 show the white light interference results of H13 steel without and with different contents of nanoparticles under the loads of 15 N and 25 N. It can be seen from Figure 8(a_1) that the worn surface of H13 steel without nanoparticles at 15 N is covered with deep furrows with large height differences. However, the worn surfaces of H13 steel with 0.02 wt.% single-phase TiC and 0.01 wt.% dual-phase TiC + TiB$_2$ nanoparticles are relatively flat and the depth of furrow is relatively uniform (Figure 8(b_1,c_1)). The wear resistance of H13 steel with 0.02 wt.% dual-phase TiC + TiB$_2$ nanoparticles is the best accompanied by the flattest surface, the smallest furrow depth and the flattest surface (Figure 8(d_1)). Figure 8(a_2,a_3) show that the depth of furrows on the surface of H13 steel without nanoparticles is large and the degree of abrasive wear is obvious. The depth of the worn surface is in the range of −3720 nm–3260 nm, and the maximum depth difference and the width of the wear scar on the worn surface can reach 6980 nm and 165 μm. Compared with H13 steel without nanoparticles, the surface abrasion of H13 steel with 0.02 wt.% single-phase TiC nanoparticles is reduced. The worn surface depth of the steel ranges from −2800 nm to 2900 nm, the maximum difference of worn surface depth is 5700 nm. Furthermore, the maximum width of the wear scar is 175 μm and the overall width of the wear scar is uniform except for the larger ones (Figure 8(b_2,b_3)). The depth of the worn surface of H13 steel with 0.01 wt.% dual-phase TiC + TiB$_2$ nanoparticles ranges from −3250 nm to 2500 nm, the maximum difference of the depth can reach 5750 nm and the maximum width of the wear scar is 135 μm. Compared to H13 steel with 0.02 wt.% single-phase TiC nanoparticles, the depth of the furrow of H13 steel with 0.01 wt.% dual-phase TiC + TiB$_2$ nanoparticles increases slightly, but the maximum width of wear scar is smaller (Figure 8(c_2,c_3)). The depth of the surface of H13 steel with 0.02 wt.% dual-phase TiC + TiB$_2$ nanoparticles ranges from −3400 nm to 2200 nm, the maximum difference of the depth of the worn surface is 5600 nm, and the depth of wear scar is reduced by 19.8%. The maximum width of the wear scar is 125 μm, and the depth is reduced by 24.2% (Figure 8(d_2,d_3)). The surface of H13 steel with 0.02 wt.% dual-phase TiC + TiB$_2$ nanoparticles has the best abrasive wear performance.
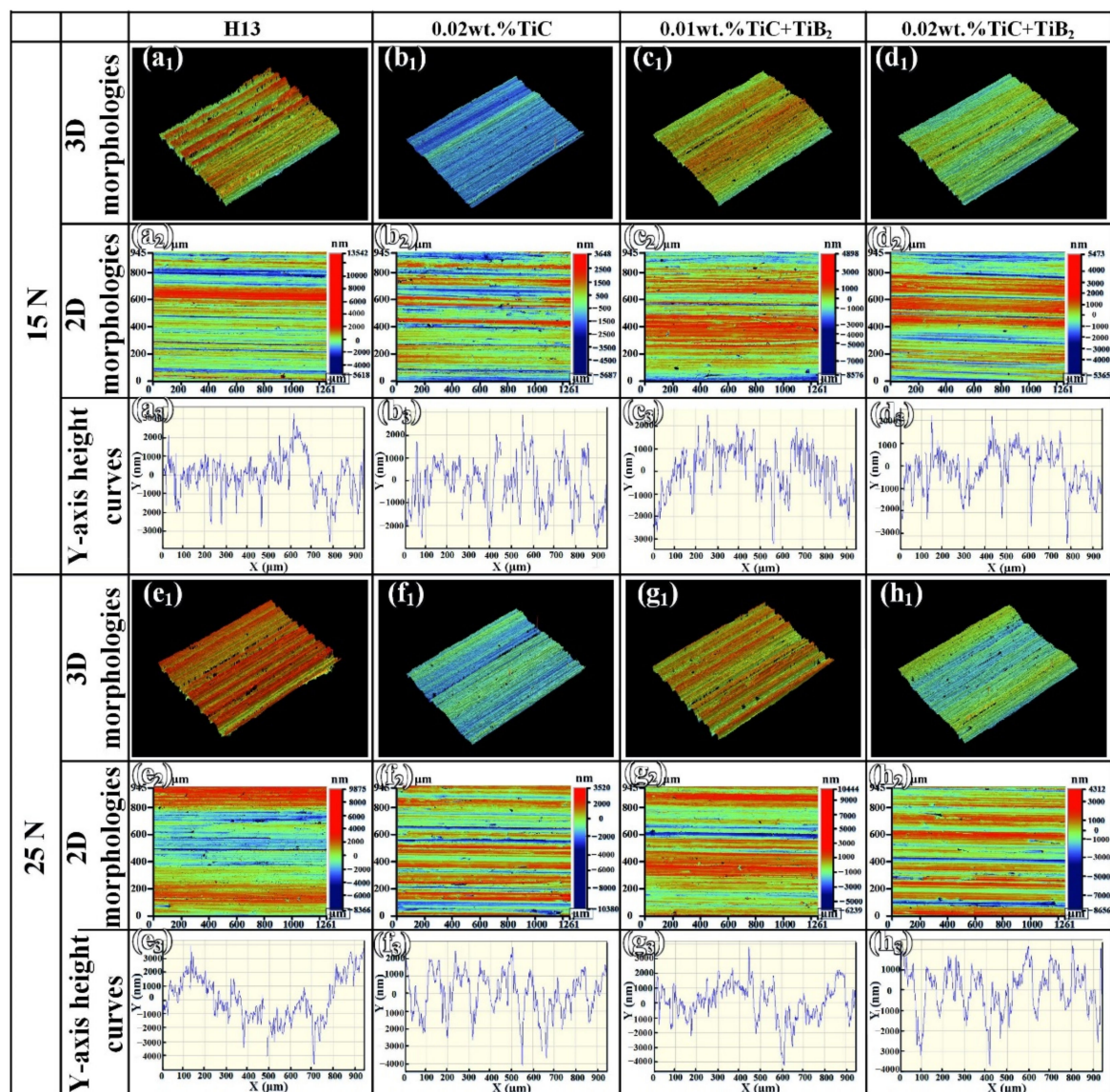
Figure 8. White light interference of worn surface of H13 steels without and with nanoparticles under sandpaper with abrasive particle size of 28 μm and different loads: (a_1–d_3) 15 N and (e_1–h_3) 25 N.

Table 4. White light interference results for different steels without and with nanoparticles under the loads of 15 N and 25 N.

Sample	The Depth of the Worn Surface (nm)		The Maximum Depth Difference (nm)		The Width of the Wear Scar (μm)	
	15 N	25 N	15 N	25 N	15 N	25 N
H13	−3720–3260	−4750–3900	6980	8650	165	165
H13 + 0.02 wt.% TiC	−2800–2900	−4200−−2500	5700	6700	175	115
H13 + 0.01 wt.%TiC + TiB_2	−3250–2500	−4250–3750	5750	8000	135	150
H13 + 0.02 wt.%TiC + TiB_2	−3400–2200	−3800–2250	5600	6050	125	90

It can be seen from the Figure 8(e_1–h_1) that increasing load can increase the depth of furrow and the degree of surface wear of the different materials. The deep furrows in Figure 8(e_1–e_3) show that the surface of H13 steel without nanoparticles at the load of 25 N is worn seriously. The range of the worn surface depth is −4750–3900 nm, the maximum difference of the depth is 8650 nm, and the wear scar reaches 165 μm. However, the ranges of worn surface depth of H13 steel with 0.02 wt.% single-phase TiC, 0.01 wt.% dual-phase TiC + TiB_2, and 0.02 wt.% dual-phase TiC + TiB_2 nanoparticles are −4200–2500 nm,

−4250–3750 nm and −3800–2250 nm and the maximum worn surface depth difference is 6700 nm, 8000 nm and 6050 nm, respectively (Figure 8(e_1–h_2)). The maximum width of the wear scars is 115 µm, 150 µm and 90 µm, respectively, which is reduced by 30.3%, 9.1% and 45.5%, respectively (Figure 8(e_3–h_3)). In summary, the degree of worn surface of the steel is reduced and the depth of the surface furrow is reduced due to the finer lath martensite of H13 steel manipulated by nanoparticles. Under the loads of 15 N and 25 N, the anti-abrasive wear order of different steels is H13 steel with 0.02 wt.% TiC + TiB_2 > H13 steel with 0.02 wt.%TiC > H13 steel with 0.01 wt.%TiC + TiB_2 > H13 steel. The H13 steel reinforced by dual-phase nanoparticles has stronger resistance to abrasive wear than that of the H13 steel reinforced by single-phase nanoparticles. The addition of nanoparticles refines the microstructure of H13 steel, especially the H13 steel with 0.02 wt.% dual-phase TiC + TiB_2, which has finer martensite and greater hardness. Therefore, it can effectively resist the intrusion of abrasive particles and reduce the generation of grooves. A similar phenomenon was also reported by Coronado et al. [76].

Figure 9 and Table 5 show the volumetric wear rate of H13 steels without and with different types and contents of nanoparticles under the load of 25 N using the sandpaper with different abrasive particle size. Rough sandpaper can increase the volume wear rate of various materials. Compared with H13 steel without nanoparticles, the volumetric wear rate of H13 steel with 0.02 wt.% TiC, 0.01 wt.% TiC + TiB_2 and 0.02 wt.% TiC + TiB_2 is reduced by 38.3%, 28.9% and 44.5%, respectively. Using the sandpaper with the abrasive particle size of 14 µm, the volumetric wear rate of H13 steel with 0.02 wt.% TiC, 0.01 wt.% and 0.02 wt.% TiC + TiB_2 is, respectively, reduced by 37.3%, 32.8% and 47.8% compared to the H13 steel. Therefore, the H13 steel with 0.02 wt.%TiC + TiB_2 shows the best wear resistance at different sandpaper size, and the anti-abrasive wear order of different steels is H13 steel with 0.02 wt.% TiC + TiB_2 > H13 steel with 0.02 wt.% TiC > H13 steel with 0.01 wt.% TiC + TiB_2 > H13 steel.
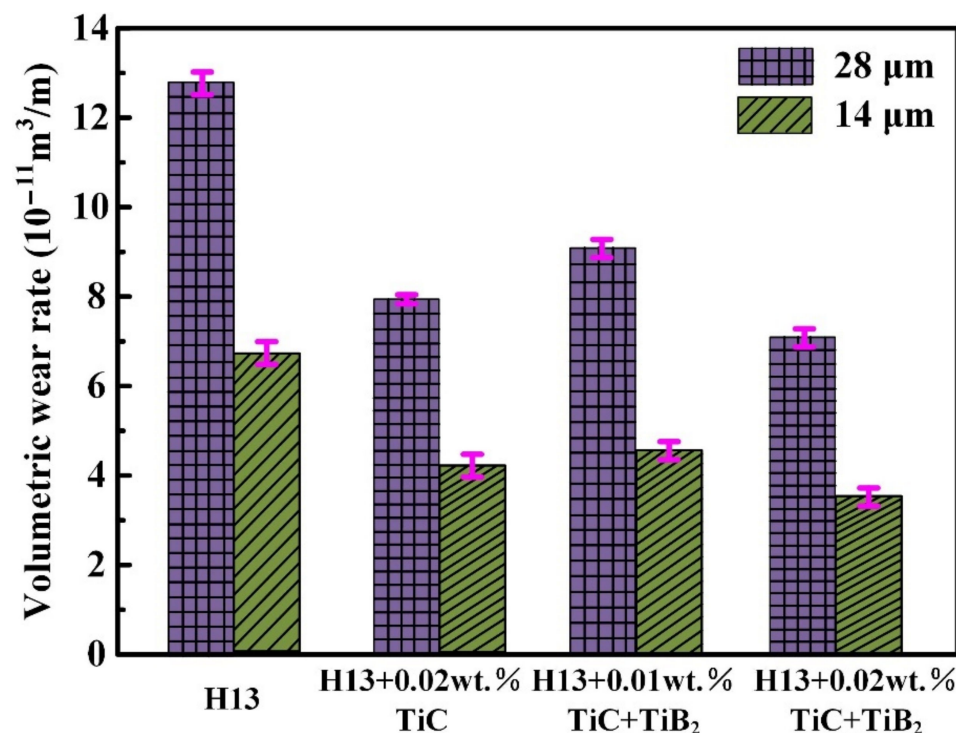

Figure 9. Volumetric wear rate of H13 steels without and with nanoparticles at different sandpaper abrasive particle sizes.

Table 5. Volumetric wear rate of H13 steels without and with nanoparticles at different sandpaper abrasive particle sizes.

Sample	Weight Loss (g)		Volumetric Wear Rate (10^{-11} m^3/m)	
	28 μm	14 μm	28 μm	14 μm
H13	0.1507 ± 0.0037	0.0789 ± 0.0029	12.8 ± 0.3	6.7 ± 0.3
H13 + 0.02 wt.% TiC	0.0930 ± 0.0011	0.0495 ± 0.0031	7.9 ± 0.1	4.2 ± 0.3
H13 + 0.01 wt.% TiC + TiB$_2$	0.1072 ± 0.0021	0.0530 ± 0.0035	9.1 ± 0.2	4.5 ± 0.2
H13 + 0.02 wt.% TiC + TiB$_2$	0.0836 ± 0.0018	0.0412 ± 0.0020	7.1 ± 0.2	3.5 ± 0.2

Figure 10a–h shows the abrasive worn surface morphologies of H13 steels without and with different contents and types of nanoparticles at the abrasive particle size of 28 μm and 14 μm. Compared with the abrasive particle size of 14 μm, the surface of the steel at the abrasive particle size of 28 μm has a higher degree of wear and the deeper furrow (Figure 10a–d). Figure 10e shows that the surface of H13 steel without nanoparticles has a more severe degree of wear, and a deeper and wider furrow. However, the degree of the surface wear of H13 steel with 0.02 wt.% TiC is reduced, and the depth and width of the furrow are also reduced (Figure 10f). Figure 10g shows that the degree of the surface wear of H13 steel with 0.01 wt.% TiC + TiB$_2$ is slighter than that of the H13 steel but is more severe than that of the H13 steel with 0.02 wt.% TiC. The H13 steel with 0.01 wt.% TiC + TiB$_2$ shows a poor wear resistance compared with the H13 steel with 0.02 wt.% TiC. In short, the H13 steel with 0.02 wt.% dual-phase TiC + TiB$_2$ has the best wear resistance.

Figure 10(e$_1$–h$_3$) and Table 6 show the white light interference results of nanoparticles of different types and contents reinforced H13 steel at the load of 25 N after abrasive wear of sandpaper with abrasive particle size of 14 μm. The corresponding results of abrasive wear of sandpaper with abrasive particle size of 28 μm are given in Figure 8(e$_1$–h$_3$). Compared with the surface with abrasive particle size of 28 μm, the number of furrows on the surface with particle sizes of 14 μm is decreased and the degree of abrasive wear is reduced. Figure 10(e$_1$–e$_3$) shows that the surface wear of H13 steel without nanoparticles is serious, accompanied by a very deep furrow, the depth of worn surface ranges from −3250 nm to 2500 nm, and the maximum difference of depth is 5750 nm. Notably, the wear scar on the worn surface reaches 150 μm. As the addition of nanoparticles, the surfaces of different H13 steels become relatively flat, the depth of the furrow is reduced, and the wear resistance is enhanced. The depth of the worn surface of H13 steel with 0.02 wt.% TiC ranges from −2300 nm to 1800 nm, the maximum difference of depth and the maximum width of the wear scar are 4100 nm and 150 μm, respectively (Figure 10(f$_1$–f$_3$)). Furthermore, the depth of the surface furrow of H13 steel with 0.01 wt.% TiC + TiB$_2$ is slightly higher than that of H13 steel with 0.02 wt.% TiC. However, compared with H13 steel without nanoparticles, the wear resistance is significantly improved. The depth of worn surface ranges from −2600 nm to 2200 nm, the maximum difference of depth and the maximum width of the wear scar is 4800 nm and 115 μm, respectively. Same as above, the H13 steel with 0.02 wt.% dual-phase TiC + TiB$_2$ has the flattest surface and the best wear resistance. The surface depth ranges from −1950 nm to 2000 nm, and the maximum difference of depth of worn surface is 3950 nm. Compared to the H13 steel, the depth of the surface of the steel manipulated by 0.02 wt.% dual-phase TiC + TiB$_2$ is reduced by 31.3%. Furthermore, the maximum width of the wear scar is 75 μm, reduced by 50%, and the depth and width of the furrow are significantly reduced. Therefore, it has the best abrasive wear resistance at the room temperature. Smaller sized abrasive particles produce more finer and more uniform furrow marks on all steel surfaces. With the increase of the abrasive size, the mass loss and wear rate of the composite increase, and the depth and width of the grooves increase, which is also confirmed by Tressia et al. [77]. Due to the irregularity of abrasive particles, larger size abrasive particles are more likely to damage and crush the surface of H13 steel and cause secondary wear. At present, the relevant literature [78] has reported the effect of

abrasive particle size on wear, but there is no unified understanding that can effectively explain its effect.
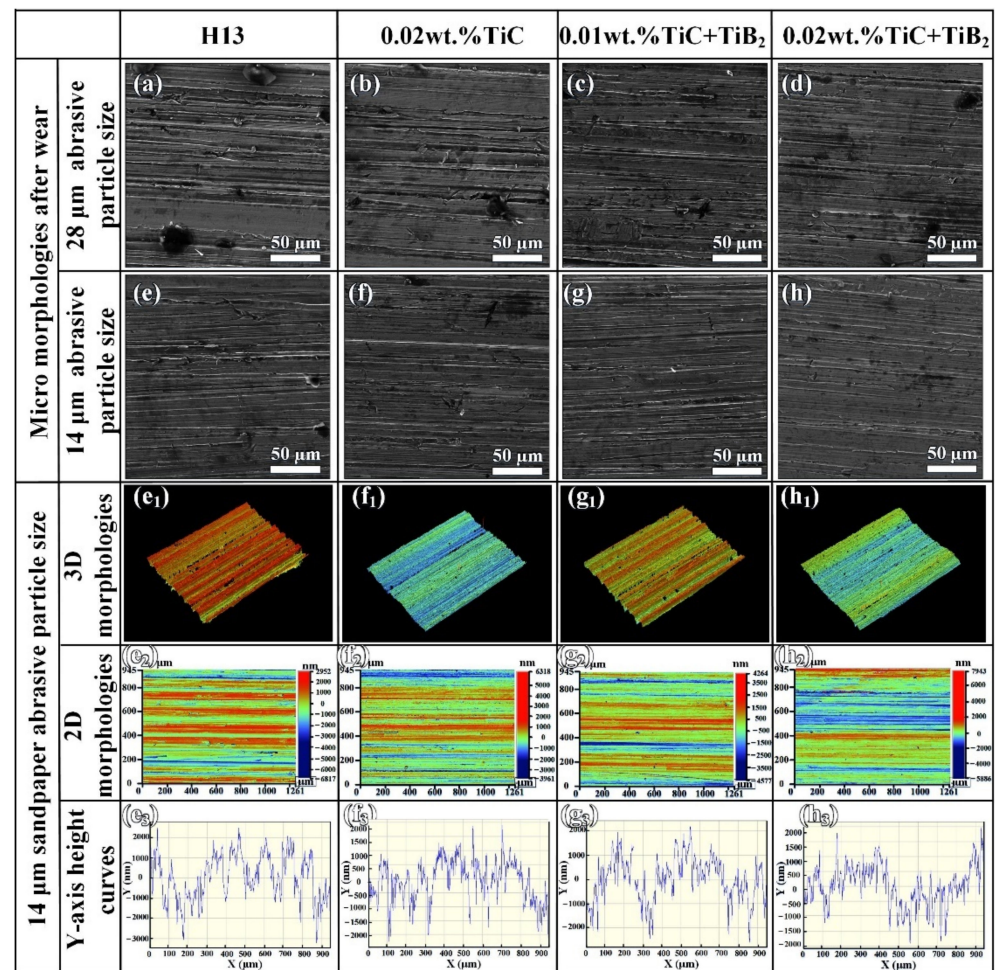
Figure 10. SEM of worn surface of H13 steels without and with nanoparticles under the load of 25 N and different sandpaper abrasive particle sizes: (**a**–**d**) 28 μm and (**e**–**h**) 14 μm, and white light interference of worn surface of H13 steel reinforced by nanoparticles under sandpaper abrasive particle sizes of 14 μm: (**e$_1$**–**e$_3$**) H13, (**f$_1$**–**f$_3$**) 0.02 wt.% TiC, (**g$_1$**–**g$_3$**) 0.01 wt.% TiC + TiB$_2$ and (**h$_1$**–**h$_3$**) 0.02 wt.% TiC + TiB$_2$.

Table 6. White light interference results for H13 steels without and with nanoparticles under sandpaper abrasive particle sizes of 14 μm and the load of 25 N.

Sample	The Depth of the Worn Surface (nm)	The Maximum Depth Difference (nm)	The Width of the Wear Scar (μm)
H13	−3250–2500	5750	150
H13 + 0.02 wt.% TiC	−2300–1800	4100	150
H13 + 0.01 wt.%TiC + TiB$_2$	−2600–2200	4800	115
H13 + 0.02 wt.%TiC + TiB$_2$	−1950–2000	3950	75

In the abrasive wear process, a furrow is formed when the matrix is plowed out under the action of friction. The addition of nanoparticles, especially dual-phase nanoparticles, can make the steel matrix resist the indentation of abrasive particles and reduce the indentation depth of abrasive particles, thus leading to the formation of denser microstructure of steel. Compared with single-phase nanoparticles, dual-phase nanoparticles have better resistance to abrasive particle invasion. The denser microstructure of H13 steel manipulated by

dual-phase nanoparticles can effectively prevent abrasive particles from being pressed into the steel, thereby protecting the matrix from excessive plowing and effectively reducing the generation of grooves.

4. Conclusions

In this work, strengthened H13 steel was prepared by adding different contents of single-phase TiC and dual-phase $TiC + TiB_2$ through the master alloy method. The tensile strength, impact toughness and abrasive wear behavior of different strengthened steels under different loads and sandpaper abrasive particle sizes at room temperature were studied. The following conclusions can be drawn:

The microstructure of H13 steel after quenching and tempering heat treatment mainly consists of tempered martensite. The microstructure of H13 steel reinforced with single-phase TiC and dual-phase $TiC + TiB_2$ nanoparticles is more uniform than that without nanoparticles. The dual-phase nanoparticles have a greater refining effect, especially when the content is 0.02 wt.%. Further, the addition of nanoparticles can effectively enhance the mechanical properties of H13 steel, including tensile performance and impact toughness. The strengthening effect of dual-phase $TiC + TiB_2$ nanoparticles is more obvious than that of single-phase TiC. Particularly, the yield strength, maximum tensile strength, fracture strain, uniform elongation, product of strength plasticity, non-notched and U-notched impact toughness of H13 steel with 0.02 wt.% dual-phase $TiC + TiB_2$ nanoparticles are 1142 MPa, 1426 MPa, 16.9%, 8.7%, 20662 MPa·%, 449.3 J/cm^2 and 41.39 J/cm^2, respectively, which increased by 11.6%, 7.6%, 14.2%, 64.2%, 26.4%, 35.0% and 33.8%, respectively, compared to H13. In addition, trace nanoparticle-reinforced H13 steel can effectively reduce the depth and width of grooves on the surface and improve the wear resistance. The volume wear rate and the depth and width of the maximum scratch of H13 steel with 0.02 wt.% dual-phase $TiC + TiB_2$ nanoparticles are 7.1×10^{-11} m^3/m, 6050 nm and 90 μm, respectively, which are reduced by 44.5%, 30.1% and 45.5%, respectively, compared with H13 steel under the load of 25 N and a sandpaper abrasive particle size of 28 μm. Dual-phase nanoparticles, especially 0.02 wt.% dual-phase $TiC + TiB_2$, can significantly improve the wear resistance of H13 steel compared to single-phase nanoparticles, which can be attributed to the denser microstructure of H13 steel manipulated by dual-phase nanoparticles, weakening the effect of ploughing wear.

Author Contributions: Conceptualization, S.-Q.K., J.-N.D. and F.C.; Data curation, J.-N.D., T.-Y.L. and F.C.; Formal analysis, S.-Q.K., J.-N.D., W.-X.W., C.-K.Z., S.-Y.W. and F.C.; Investigation, S.-Q.K., J.-N.D., W.-X.W., T.-Y.L. and F.C.; Supervision, J.-N.D. and F.C.; Writing—review and editing, S.-Q.K., J.-N.D. and F.C. All authors have read and agreed to the published version of the manuscript.

Institutional Review Board Statement: Not applicable.

Informed Consent Statement: Not applicable.

Data Availability Statement: Data sharing is not applicable.

References

1. Ma, K.J.; Stankus, J. Case study and design of steel set support for aged belt entry rehabilitation. *Int. J. Min. Sci. Technol.* **2018**, *28*, 101–106. [CrossRef]
2. Zhenjun, S.; Porter, I.; Nemcik, J.; Baafi, E. Comparing the reinforcement capacity of welded steel mesh and a thin spray-on liner using large scale laboratory tests. *Int. J. Min. Sci. Technol.* **2014**, *24*, 373–377. [CrossRef]
3. Li, X.; Lin, J.; Xia, Z.; Zhang, Y.; Fu, H. Influence of Deposition Patterns on Distortion of H13 Steel by Wire-Arc Additive Manufacturing. *Metals* **2021**, *11*, 485. [CrossRef]

4. Yang, H.-Y.; Yan, Y.-F.; Liu, T.-S.; Dong, B.-X.; Chen, L.-Y.; Shu, S.-L.; Qiu, F.; Jiang, Q.-C.; Zhang, L.-C. Unprecedented enhancement in strength-plasticity synergy of (TiC+Al₆MoTi+Mo)/Al cermet by multiple length-scale microstructure stimulated synergistic deformation. *Compos. B Eng.* **2021**, *225*, 109265. [CrossRef]

5. Qiu, F.; Liu, T.-S.; Zhang, X.; Chang, F.; Shu, S.-L.; Yang, H.-Y.; Zhao, Q.-L.; Jiang, Q.-C. Application of nanoparticles in cast steel: An overview. *China Foundry* **2020**, *17*, 111–126. [CrossRef]

6. Saucedo-Muñoz, M.L. Precipitation kinetics of carbides during cyclical and isothermal aging of 2.25Cr–1Mo steel and its effect on mechanical properties. *J. Iron Steel Res. Int.* **2021**, *28*, 1282–1290. [CrossRef]

7. Chang, F.; Zhang, H.; Gao, Y.-L.; Shu, S.-L.; Qiu, F.; Jiang, Q.-C. Microstructure evolution and mechanical property enhancement of high-Cr hot work die steel manipulated by trace amounts of nano-sized TiC. *Mater. Sci. Eng. A-Struct.* **2021**, *824*, 141788. [CrossRef]

8. Xu, T.; Song, G.; Yang, Y.; Ge, P.-X.; Tang, L.-X. Visualization and simulation of steel metallurgy processes. *Int. J. Miner. Metall. Mater.* **2021**, *28*, 1387. [CrossRef]

9. Li, Y.; Zeng, Y.-P.; Wang, Z.-C. Interfacial microstructure evolution of 12Cr1MoV/TP347H dissimilar steel welded joints during aging. *Int. J. Miner. Metall. Mater.* **2021**, *28*, 1497. [CrossRef]

10. Zhang, J.-J.; Zhai, B.-Y.; Zhang, L.; Wang, W.-l. A comparison study on interfacial properties of fluorine-bearing and fluorine-free mold flux for casting advanced high-strength steels. *J. Iron Steel Res. Int.* **2022**, 1–6. [CrossRef]

11. Liu, Y.; Sun, Y.-H.; Wu, H.-T. Effects of chromium on the microstructure and hot ductility of Nb-microalloyed steel. *Int. J. Miner. Metall. Mater.* **2021**, *28*, 1011. [CrossRef]

12. Srivastava, G.K.; Vemavarapu, M.S.R.M. Drillability prediction in some metamorphic rocks using composite penetration rate index (CPRI)—An approach. *Int. J. Min. Sci. Technol.* **2021**, *31*, 631–641. [CrossRef]

13. Huang, Y.; Cheng, G.; Zhu, M. Effect of Ti Content on the Behavior of Primary Carbides in H13 Ingots. *Metals* **2020**, *10*, 837. [CrossRef]

14. Han, X.; Zhang, Z.; Wang, B.; Thrush, S.J.; Barber, G.C.; Qiu, F. Microstructures, compressive residual stress, friction behavior, and wear mechanism of quenched and tempered shot peened medium carbon steel. *Wear* **2022**, *488*, 204131. [CrossRef]

15. Yang, H.-Y.; Wang, Z.; Yue, X.; Ji, P.-J.; Shu, S.-L. Simultaneously improved strength and toughness of in situ bi-phased TiB₂-Ti(C,N)-Ni cermets by Mo addition. *J. Alloys Compd.* **2020**, *820*, 153068. [CrossRef]

16. Mohalik, N.K.; Mandal, S.; Ray, S.K.; Khan, A.M.; Mishra, D.; Pandey, J.K. TGA/DSC study to characterise and classify coal seams conforming to susceptibility towards spontaneous combustion. *Int. J. Min. Sci. Technol.* **2021**, *32*, 75–88. [CrossRef]

17. Zhao, X.; Hai, X. Microstructure and tribological behavior of the nickel-coated-graphite-reinforced Babbitt metal composite fabricated via selective laser melting. *Int. J. Miner. Metall. Mater.* **2022**, *29*, 320–326. [CrossRef]

18. Zhou, Y.; Jiang, W. Effect of sliding speed on elevated-temperature wear behavior of AISI H13 steel. *J. Iron Steel Res. Int.* **2021**, *28*, 1180–1189. [CrossRef]

19. Zhao, Y.; Liu, N.; Zheng, X.; Zhang, N. Mechanical model for controlling floor heave in deep roadways with U-shaped steel closed support. *Int. J. Min. Sci. Technol.* **2015**, *25*, 713–720. [CrossRef]

20. Han, X.; Zhang, Z.; Hou, J.; Barber, G.C.; Qiu, F. Tribological behavior of shot peened/austempered AISI 5160 steel. *Tribol. Int.* **2020**, *145*, 106197. [CrossRef]

21. Kang, C.-P.; Liu, F.-B.; Zheng, H.-B.; Li, H.-B.; Jiang, Z.-H.; Chen, K.; Suo, H.-Y.; Yu, X.-H. Microstructure evolution and mechanical properties of PESR 55Cr17Mo1VN plastic die steel during quenching and tempering treatment. *J. Iron Steel Res. Int.* **2021**, *28*, 1625–1633. [CrossRef]

22. Zhao, F.; He, G.-N.; Liu, Y.-Z.; Zhang, Z.-H.; Xie, J.-X. Effect of titanium microalloying on microstructure and mechanical properties of vanadium microalloyed steels for hot forging. *J. Iron Steel Res. Int.* **2021**, 1–12. [CrossRef]

23. Li, C.-S.; Li, B.-Z.; Jin, X.; Wang, Y. Microstructure and mechanical properties in core of a carburizing 20CrNi2MoV bearing steel subjected to cryogenic treatment. *J. Iron Steel Res. Int.* **2021**, *28*, 360–369. [CrossRef]

24. Cai, W.; Chang, Z.; Zhang, D.; Wang, X.; Cao, W.; Zhou, Y. Roof filling control technology and application to mine roadway damage in small pit goaf. *Int. J. Min. Sci. Technol.* **2019**, *29*, 477–482. [CrossRef]

25. Li, C.-L.; Qiu, F.; Chang, F.; Zhao, X.-M.; Geng, R.; Yang, H.-Y.; Zhao, Q.-L.; Jiang, Q.-C. Simultaneously Enhanced Strength, Toughness and Ductility of Cast 40Cr Steels Strengthened by Trace Biphase TiCₓ-TiB₂ Nanoparticles. *Metals* **2018**, *8*, 707. [CrossRef]

26. Chen, L.-Y.; Liang, S.-X.; Liu, Y.; Zhang, L.-C. Additive manufacturing of metallic lattice structures: Unconstrained design, accurate fabrication, fascinated performances, and challenges. *Mater. Sci. Eng. R-Rep.* **2021**, *146*, 100648. [CrossRef]

27. Yang, X.-H.; Chen, X.-H.; Pan, S.-W.; Wang, Z.-D.; Chen, K.-X.; Li, D.-Y.; Qin, J.-W. Microstructure and mechanical properties of ultralow carbon high-strength steel weld metals with or without Cu−Nb addition. *Int. J. Miner. Metall. Mater.* **2021**, *28*, 120. [CrossRef]

28. Zhu, J.; Zhang, Z.-H.; Xie, J.-X. Relationship between martensite microstructure and ductility of H13 steel from aspect of crystallography. *J. Iron Steel Res. Int.* **2021**, *28*, 1268–1281. [CrossRef]

29. Qiu, G.-X.; Zhan, D.-P.; Cao, L.; Zhang, H.-S. Effect of zirconium on inclusions and mechanical properties of China low activation martensitic steel. *J. Iron Steel Res. Int.* **2021**, *28*, 1168–1179. [CrossRef]

30. Le, Z.; Yu, Q.; Zhu, W.; Liu, H.; Yang, T. Experimental study on the effect of granular backfill with various gradations on the mechanical behavior of rock. *Int. J. Min. Sci. Technol.* **2021**, *31*, 889–899. [CrossRef]

31. Zhou, J.-H.; Shen, Y.-F.; Jia, N. Strengthening mechanisms of reduced activation ferritic/martensitic steels: A review. *Int. J. Miner. Metall. Mater.* **2021**, *28*, 335. [CrossRef]

32. Lin, L.; Zeng, J.-Q. Consideration of green intelligent steel processes and narrow window stability control technology on steel quality. *Int. J. Miner. Metall. Mater.* **2021**, *28*, 1264. [CrossRef]

33. Zhang, H.; Wang, W.-X.; Chang, F.; Li, C.-L.; Shu, S.-L.; Wang, Z.-F.; Han, X.; Zou, Q.; Qiu, F.; Jiang, Q. Microstructure manipulation and strengthening mechanisms of 40Cr steel via trace TiC nanoparticles. *Mater. Sci. Eng. A-Struct.* **2021**, *822*, 141693. [CrossRef]

34. Zheng, G.Y.; Luo, X.; Huang, B.; Li, P.T.; Yang, Y.Q. Distributions of grains and precipitates in gradient lamellae Al-Zn-Mg-Cu alloy by ultrasonic surface rolling processing. *Mater. Sci. Eng. A-Struct.* **2021**, *825*, 141911. [CrossRef]

35. Qu, T.-P.; Wang, D.-Y.; Wang, H.-H.; Hou, D.; Tian, J.; Hu, S.-Y.; Su, L.-J. Interface characteristics between TiN and matrix and their effect on solidification structure. *J. Iron Steel Res. Int.* **2021**, *28*, 1149–1158. [CrossRef]

36. Huang, Y.; Liu, W.-N.; Zhao, A.-M.; Han, J.-K.; Wang, Z.-G.; Yin, H.-X. Effect of Mo content on the thermal stability of Ti–Mo-bearing ferritic steel. *Int. J. Miner. Metall. Mater.* **2021**, *28*, 412. [CrossRef]

37. Li, S.-Y.; Qin, S.-Y.; Xi, X.-J.; Sun, G.-Y.; Yang, W.-S.; Guo, J.; Guo, H.-J. Solidified Structure Refinement of H13 Tool Steel under a Multi-Rotational Speed Super Gravity Field. *Metals* **2020**, *10*, 1428. [CrossRef]

38. Luo, X.; Yang, L.; Zhao, A.W.; Lu, W.J.; Gan, B.; Yang, Y.Q. Al_2O_3 nanoparticle reinforced heterogeneous CrCoNi-matrix composites with improved strength-ductility synergy. *Mater. Sci. Eng. A-Struct.* **2022**, *832*, 142398. [CrossRef]

39. Liu, D.-K.; Yang, J.; Zhang, Y.-H.; Xu, L.-Y. Effect of Mo content on nano-scaled particles, prior austenite grains and impact toughness of CGHAZ in offshore engineering steels. *J. Iron Steel Res. Int.* **2021**, 1–13. [CrossRef]

40. Liu, R.-Z.; Gu, W.-W.; Yang, Y.; Lu, Y.; Tan, H.-B.; Yang, J.-F. Microstructure and mechanical properties of reaction-bonded B4C–SiC composites. *Int. J. Miner. Metall. Mater.* **2021**, *28*, 1828. [CrossRef]

41. Li, H.; Ji, H.; Cui, X.; Che, X.; Zhang, Q.; Zhong, J.; Jin, R.; Wang, L.; Luo, Y. Kinetics, thermodynamics, and equilibrium of As(III), Cd(II), Cu(II) and Pb(II) adsorption using porous chitosan bead-supported $MnFe_2O_4$ nanoparticles. *Int. J. Min. Sci. Technol.* **2021**, *31*, 1107–1115. [CrossRef]

42. Wang, B.; Qiu, F.; Cui, W.; Jin, Y.; Zhang, Y.; Hu, Z.; Barber, G.C. Microstructure and Tensile Properties of Graphite Ductile Iron Improved by Minor Amount of Dual-Phased TiC-TiB_2 Nanoparticles. *Adv. Eng. Mater.* **2021**, *23*, 2100246. [CrossRef]

43. Qian, F.; Li, H.-L.; Yang, W.-G.; Guo, H.-R.; Liu, G.-Q.; Li, H.-X.; Ma, B.-Y. Corrosion resistance of BN–ZrO_2 ceramics with different additives by molten steel. *J. Iron Steel Res. Int.* **2022**, 1–9. [CrossRef]

44. Liu, T.-S.; Qiu, F.; Dong, B.-X.; Geng, R.; Zha, M.; Yang, H.-Y.; Shu, S.-L.; Jiang, Q.-C. Role of trace nanoparticles in establishing fully optimized microstructure configuration of cold-rolled Al alloy. *Mater Design.* **2021**, *206*, 109743. [CrossRef]

45. Li, Q.; Dong, B.-X.; Liu, T.-S.; Yang, H.-Y.; Shu, S.-L.; Qiu, F.; Jiang, Q.-C. Insight into solidification microstructure control by trace $TiCN$-TiB_2 particles for yielding fine-tuned nanoprecipitates in a hypoeutectic Al-Si-Mg alloy. *Mater. Sci. Eng. A-Struct.* **2021**, *827*, 142093. [CrossRef]

46. Zhu, L.; Liu, T.-S.; Duan, T.-T.; Li, T.-T.; Qiu, F.; Yang, H.-Y.; Bai, Z.-H.; Liu, Y.-Y.; Jiang, Q.-C. Design of a new Al-Cu alloy manipulated by in-situ nanocrystals with superior high temperature tensile properties and its constitutive equation. *Mater. Design.* **2019**, *181*, 107945. [CrossRef]

47. Fu, Z.-X.; Yang, G.-W.; Han, R.-Y.; Xu, Y.-W.; Mao, X.-P.; Bao, S.-Q.; Zhao, G. Influence of coiling temperature on microstructure and mechanical properties of a hot-rolled high-strength steel microalloyed with Ti, Mo and V. *J. Iron Steel Res. Int.* **2021**. [CrossRef]

48. Kiahosseini, S.R.; Ahmadian, H. Effect of residual structural strain caused by the addition of Co_3O_4 nanoparticles on the structural, hardness and magnetic properties of an Al/Co_3O_4 nanocomposite produced by powder metallurgy. *Int. J. Miner. Metall. Mater.* **2020**, *27*, 384. [CrossRef]

49. Yang, H.; Yue, X.; Wang, Z.; Shao, Y.; Shu, S. Strengthening mechanism of TiC/Al composites using Al-Ti-C/CNTs with doping alloying elements (Mg, Zn and Cu). *J. Mater. Res. Technol-JMRT.* **2020**, *9*, 6475–6487. [CrossRef]

50. Li, Q.; Qiu, F.; Dong, B.-X.; Gao, X.; Shu, S.-L.; Yang, H.-Y.; Jiang, Q.-C. Processing, multiscale microstructure refinement and mechanical property enhancement of hypoeutectic Al-Si alloys via in situ bimodal-sized TiB_2 particles. *Mater. Sci. Eng. A-Struct.* **2020**, *777*, 139081. [CrossRef]

51. Yang, H.-Y.; Cai, Z.-J.; Zhang, Q.; Shao, Y.; Dong, B.-X.; Xuan, Q.-Q.; Qiu, F. Comparison of the effects of Mg and Zn on the interface mismatch and compression properties of 50 vol% TiB_2/Al composites. *Ceram. Int.* **2021**, *47*, 22121–22129. [CrossRef]

52. Zhang, J.-W.; Cao, Y.-G.; Zhang, C.-G.; Li, Z.-D.; Wang, W.-X. Effect of Nb addition on microstructure and mechanical properties of 25CrNiMoV (DZ2) steel for high-speed railway axles. *J. Iron Steel Res. Int.* **2021**. [CrossRef]

53. Shi, R.-J.; Wang, Z.-D.; Qiao, L.-J.; Pang, X.-L. Effect of in-situ nanoparticles on the mechanical properties and hydrogen embrittlement of high-strength steel. *Int. J. Miner. Metall. Mater.* **2021**, *28*, 644. [CrossRef]

54. Zang, J.; Dai, P.; Yang, Y.; Liu, S.; Huang, B.; Ru, J.; Luo, X. Study on the Relationship between High Temperature Mechanical Properties and Precipitates Evolution of 7085 Al Alloy after Long Time Thermal Exposures. *Metals* **2021**, *11*, 1483. [CrossRef]

55. Lu, T.-X.; Chen, C.-G.; Guo, Z.-M.; Li, P.; Guo, M.-X. Tungsten nanoparticle-strengthened copper composite prepared by a sol-gel method and in-situ reaction. *Int. J. Miner. Metall. Mater.* **2019**, *26*, 1477. [CrossRef]

56. Gómez-Esparza, C.D.; Duarte-Moller, A.; León, C.L.-D.D.; Martínez-Sánchez, R.; Hernández-Paz, J.F.; Rodríguez-González, C.A. Influence of ZnO nanoparticles on the microstructure of a CoCrFeMoNi matrix via powder metallurgy. *Int. J. Miner. Metall. Mater.* **2019**, *26*, 1467. [CrossRef]

57. Wang, S.; Wu, G.; Mao, X. Titanium microalloying in steel: A review of its effects on processing, microstructure and mechanical properties. *Int. J. Miner. Metall. Mater.* **2021**. [CrossRef]

58. Zhu, L.; Qiu, F.; Qiu, D.; Duan, T.-T.; Chang, F.; Li, T.-T.; Shu, S.-L.; Yang, H.-Y.; He, Y.; Jiang, Q.-C. Efficient microstructure refinement of Al-Si-Mg alloy manipulated by nanocrystals formed by in-situ crystallization in melt. *Mater. Sci. Eng. A-Struct.* **2019**, *751*, 90–98. [CrossRef]

59. Kou, S.-Q.; Gao, Y.-L.; Song, W.; Zhao, H.-L.; Guo, Y.-B.; Zhang, S.; Yang, H.-Y. Compression properties and work-hardening behavior of the NiAl matrix composite reinforced with in situ TaC ceramic particulates. *Vacuum* **2021**, *186*, 110035. [CrossRef]

60. Zhu, L.; Qiu, F.; Zou, Q.; Han, X.; Shu, S.-L.; Yang, H.-Y.; Jiang, Q.-C. Multiscale design of alpha-Al, eutectic silicon and Mg2Si phases in Al-Si-Mg alloy manipulated by in situ nanosized crystals. *Mater. Sci. Eng. A-Struct.* **2021**, *802*, 140627. [CrossRef]

61. Wang, B.; Zhang, Y.; Qiu, F.; Cai, G.; Cui, W.; Hu, Z.; Zhang, H.; Tyrer, N.; Barber, G.C. Role of trace nanoparticles in manipulating the widmanstatten structure of low carbon steel. *Mater. Lett.* **2022**, *306*, 130853. [CrossRef]

62. Geng, R.; Qiu, F.; Jiang, Q.-C. Reinforcement in Al Matrix Composites: A Review of Strengthening Behavior of Nano-Sized Particles. *Adv. Eng. Mater.* **2018**, *20*, 1701089. [CrossRef]

63. Chen, R.; Wang, Z.; He, J.; Zhu, F.; Li, C. Effects of Rare Earth Elements on Microstructure and Mechanical Properties of H13 Die Steel. *Metals* **2020**, *10*, 918. [CrossRef]

64. Qiu, F.; Zhang, H.; Li, C.-L.; Wang, Z.-F.; Chang, F.; Yang, H.-Y.; Li, C.-D.; Han, X.; Jiang, Q.-C. Simultaneously enhanced strength and toughness of cast medium carbon steels matrix composites by trace nano-sized TiC particles. *Mater. Sci. Eng. A-Struct.* **2021**, *819*, 141485. [CrossRef]

65. Wang, B.; Qiu, F.; Zhang, Y.; Yang, J.; Cui, W.; Jin, Y.; Cai, G.; Yuan, Y.; Guo, S.; Li, H.; et al. Influences of dual-phased nanoparticles on microstructure, mechanical properties and wear resistance of vermicular graphite cast iron. *Mater. Lett.* **2022**, *308*, 131296. [CrossRef]

66. Wang, G.; Li, Y.; Wang, E.; Huang, Q.; Wang, S.; Li, H. Experimental study on preparation of nanoparticle-surfactant nanofluids and their effects on coal surface wettability. *Int. J. Min. Sci. Technol.* **2022**. [CrossRef]

67. Li, Y.; Bian, X.; Liu, Y.; Wu, W.; Fu, G. Synthesis and characterization of ceria nanoparticles by complex-precipitation route. *Int. J. Miner. Metall. Mater.* **2022**, *29*, 292–297. [CrossRef]

68. Wang, X.; Li, G.; Liu, Y.; Cao, Y.; Wang, F.; Wang, Q. Investigation of Primary Carbides in a Commercial-Sized Electroslag Remelting Ingot of H13 Steel. *Metals* **2019**, *9*, 1247. [CrossRef]

69. Wang, B.; Qiu, F.; Barber, G.C.; Zou, Q.; Wang, J.; Guo, S.; Yuan, Y.; Jiang, Q. Role of nano-sized materials as lubricant additives in friction and wear reduction: A review. *Wear* **2022**, *490-491*, 204–206. [CrossRef]

70. Sakthivel, S.; Prasanna Venkatesh, R. Solid state synthesis of nano-mineral particles. *Int. J. Min. Sci. Technol.* **2012**, *22*, 651–655. [CrossRef]

71. Dong, B.-X.; Ma, X.-D.; Liu, T.-S.; Li, Q.; Yang, H.-Y.; Shu, S.-L.; Zhang, B.-Q.; Qiu, F.; Jiang, Q.-C. Reaction behaviors and specific exposed crystal planes manipulation mechanism of TiC nanoparticles. *J. Am. Ceram. Soc.* **2021**, *104*, 2820–2835. [CrossRef]

72. Luo, X.; Huang, B.; Guo, X.; Lu, W.; Zheng, G.; Huang, B.; Li, J.; Li, P.; Yang, Y. High ZT Value of Pure SnSe Polycrystalline Materials Prepared by High-Energy Ball Milling plus Hot Pressing Sintering. *ACS Appl. Mater. Interfaces* **2021**, *13*, 43011–43021. [CrossRef] [PubMed]

73. Dong, B.-X.; Li, Q.; Wang, Z.-F.; Liu, T.-S.; Yang, H.-Y.; Shu, S.-L.; Chen, L.-Y.; Qiu, F.; Jiang, Q.-C.; Zhang, L.-C. Enhancing strength-ductility synergy and mechanisms of Al-based composites by size-tunable in-situ TiB$_2$ particles with specific spatial distribution. *Compos. B Eng.* **2021**, *217*, 108912. [CrossRef]

74. Yang, H.-Y.; Wang, Z.; Chen, L.-Y.; Shu, S.-L.; Qiu, F.; Zhang, L.-C. Interface formation and bonding control in high-volume-fraction (TiC+TiB$_2$)/Al composites and their roles in enhancing properties. *Compos. B Eng.* **2021**, *209*, 108605. [CrossRef]

75. Dong, B.-X.; Li, Q.; Yang, H.-Y.; Liu, T.-S.; Qiu, F.; Shu, S.-L.; Jiang, Q.-C.; Zhang, L.-C. Synergistic optimization in solidification microstructure and mechanical performance of novel (TiC$_x$N$_y$−TiB$_2$)$_p$/Al nanocomposites: Design, tuning and mechanism. *Compos. Part A-Appl. S* **2022**, *155*, 106843. [CrossRef]

76. Coronado, J.J.; Sinatora, A. Effect of abrasive size on wear of metallic materials and its relationship with microchips morphology and wear micromechanisms: Part 1. *Wear* **2011**, *271*, 1794–1803. [CrossRef]

77. Tressia, G.; Penagos, J.J.; Sinatora, A. Effect of abrasive particle size on slurry abrasion resistance of austenitic and martensitic steels. *Wear* **2017**, *376*, 63–69. [CrossRef]

78. Chacon-Nava, J.G.; Martinez-Villafañe, A.; Almeraya-Calderon, F.; Cabral-Miramontes, J.A.; Stack, M.M. Some remarks on particle size effects on the abrasion of a range of Fe based alloys. *Tribol. Int.* **2010**, *43*, 1307–1317. [CrossRef]